Supplementary material: Synthesis and crystal structure of acentric anhydrous beryllium carbonate Be(CO$_3$)

Dominik Spahr[*,a], Lkhamsuren Bayarjargal[a], Elena Bykova[a], Maxim Bykov[b], Tim H. Reuter[a], Lukas Brüning[b], Pascal L. Jurzick[c], Lena Wedek[a], Victor Milman[d], Björn Wehinger[e], Björn Winkler[a]

[a]*Goethe University Frankfurt, Institute of Geosciences, Altenhöferallee 1, 60438 Frankfurt, Germany*
[b]*Goethe University Frankfurt, Institute of Inorganic and Analytical Chemistry, Max-von-Laue-Straße 7, 60438 Frankfurt, Germany*
[c]*University of Cologne, Institute of Inorganic Chemistry, Greinstraße 6, 50939 Cologne, Germany*
[d]*Dassault Systèmes BIOVIA, 334 Cambridge Science Park, Cambridge CB4 0WN, United Kingdom*
[e]*European Synchrotron Radiation Facility ESRF, 71 avenue des Martyrs, CS40220, 38043 Grenoble Cedex 9, France*

1. Methods

1.1. Sample material

The high-pressure experiments were performed using commercial beryllium oxide (BeO) powder (99.95% purity, ThermoFischer GmbH, Kandel, Germany). The BeO powder was used without further purification. Prior to loading, the powder was compacted between a diamond and a glass plate to obtain a 10–20 µm thin powder compact. We used Raman spectroscopy to confirm the phase purity of the powder compact before the cryogenic loading. The experimental Raman spectrum of BeO is accurately reproduced by the DFT calculations in space group $P6_3mc$ (Fig. S 1).[1] We observed no additional Raman modes in the experimental Raman spectra.
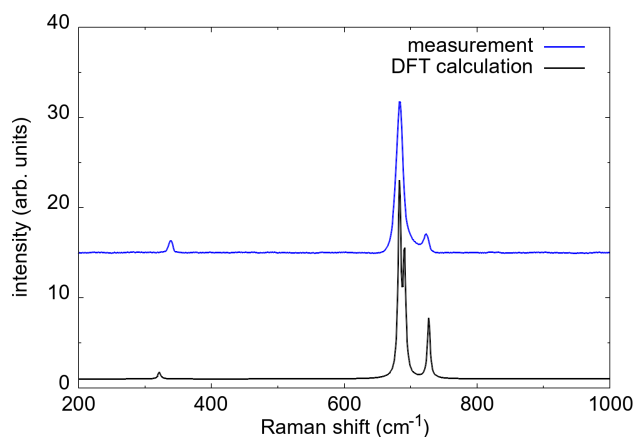

Figure S 1: Experimental Raman spectrum of BeO powder before the cryogenic loading in comparison with the DFT-based calculation. The calculated Raman shifts were rescaled by 2 %.

The CO$_2$ gas for the gas-jet was used as purchased (Nippon gases, purity $\geq$ 99.995%).

1.2. High-pressure experiments

The high-pressure experiments were carried out in Boehler-Almax type diamond anvil cells (DACs).[2] We used diamonds with 70° opening angle on both sides and 300 µm culet size. The Re-gaskets, which were pre-indented to a thickness of $\approx$ 50 µm, and gasket holes with $\approx$ 100 µm diameter were drilled with a custom-built laser

set-up. Afterwards, the powder compact with dimensions of $\approx 80 \times 60$ µm^2 and a thickness of 10–20 µm was placed in the gasket hole on the culet of the bottom diamond. In addition, a ruby chip for pressure determination was added. The pressure was determined by measuring the shift of the ruby fluorescence and we assume an error of 6% due to non-hydrostatic conditions.[3]

CO$_2$ dry-ice was directly condensed into the gasket hole using a custom-built cryogenic loading system (see Spahr *et al.*[4]) derived from an earlier concept.[5] The DAC was opened and placed on a liquid nitrogen cooled Cu-holder, which was cooled down to $\approx$ 100 K. We used a small nozzle to align the CO$_2$ gas jet with 5 l min^{-1} directly on the gap between upper diamond and the gasket. The precipitation of the CO$_2$ in the gasket hole was monitored using an optical microscope and a camera. After a sufficient amount of CO$_2$ was gathered in the gasket hole, the DAC was tightly closed.

1.3. Laser heating

The sample was laser-heated from one side using a custom-built set-up equipped with a Coherent Diamond K-250 pulsed CO$_2$ laser ($\lambda = 10600$ nm).[6] The laser power was adjusted to achieve a coupling of the laser to the sample, using a laser power of $\leq$ 1 W, resulting in a maximum temperature of $T_{\max} = 1500(200)$ K. The temperatures were determined by the two-color pyrometer method, employing Planck and Wien fits.[7] The heating time was $\approx$ 60 min. It is well established that laser-heating in DACs always suffers from large temperature gradients and the actual temperature is strongly dependent on the coupling of the laser with the sample, especially at lower temperatures. We estimate an uncertainty of at least $\pm 15\%$ of the nominal temperature in the laser-heated region depending on the focus of the laser beam, based on typical 2D temperature-gradient determination experiments performed in DACs.[8]

1.4. Raman spectroscopy

Raman spectroscopy at high pressures and at ambient conditions was performed using an Oxford Instruments WITec alpha 300R Raman imaging microscope. The Raman microscope was equipped with an Olympus SLMPan N 50$\times$ objective. The measurements were performed with a 532 nm laser. We used the 1800 grooves mm^{-1} grating

of the WITec UHTS 300S (VIS-NIR) spectrograph in combination with an Andor DR316B-LDC-DD CCD detector. The applied laser power was 100 mW on the sample and the spot size of the Raman laser was ≈ 0.8 μm. We assume a depth resolution of ≈ 6 μm in the direction of the laser beam. Raman maps were measured on a grid with a step-size of 1 μm. The background of the Raman spectra was corrected using the software package Fityk.[9]

1.5. Single crystal synchrotron X-ray diffraction

Single crystal synchrotron X-ray diffraction was carried out at the ESRF in Grenoble, France, at the high-pressure beam line ID27.[10] The beam size on the sample was 0.7×0.7 μm^2, focused by Kirkpatrick Baez mirrors. The diffraction data were collected using an Eiger2 X 9M CdTe detector, a wavelength of 0.3738 Å (33.2 keV) and a detector to sample distance of 190 mm. We rotated the DAC by $\pm 33°$ around the vertical axis perpendicular to the beam while collecting frames in 0.5° steps with 2 s acquisition time per frame.

The detector to sample distance was calibrated using the powder diffraction pattern of a CeO$_2$ standard in conjunction with the software DIOPTAS.[11] The diffractometer/detector geometry for the analysis of the single crystal diffraction data was calibrated using diffraction data collected from a vanadinite (Pb$_5$(VO$_4$)$_3$Cl) single crystal in a DAC at ambient pressure. After the data collection, the reflections were indexed and integrated employing CrysAlis^{PRO} (version 43.67a).[12] We used the Domain Auto Finder program (DAFi) to find possible single crystal domains for the subsequent data reduction.[13] The structure solution and refinement were performed using the software package OLEX2 employing SHELXT for the crystal structure determination and SHELX for the refinement.[14,15,16]

1.6. Second harmonic generation measurements

Second harmonic generation (SHG) measurements were performed using a custom-built set-up.[17] For the generation of the fundamental pump wave we used an Impex HighTech Q-switched Nd:YAG laser (1064 nm, 5–6 ns, 2 kHz). The fundamental infrared light was separated from the generated second harmonic (532 nm) with a harmonic separator, a short-pass filter, and an interference filter. The SHG signal was collected using a photomultiplier tube (Hamamatsu R2949) in combination with an oscilloscope (Tektronix TDS2022). The samples were measured in transmission geometry using the Kurtz-Perry approach.[18] Quartz (SiO$_2$), corundum (Al$_2$O$_3$) and BeO powders outside a DAC at ambient conditions were employed as reference materials. Be(CO$_3$) was measured in a DAC. For the samples in the DAC and the reference materials 40 individual SHG measurements were carried out and averaged. Background signals between the laser pulses were used to correct the measured SHG intensities using a Matlab script.

1.7. Density functional theory-based calculations

First-principles calculations were carried out within the framework of density functional theory (DFT), employing the Perdew-Burke-Ernzerhof (PBE) exchange-correlation functional and the plane wave/pseudopotential approach implemented in the CASTEP simulation package.[19,20,21] "On the fly" norm-conserving or ultrasoft pseudopotentials generated using the descriptors in the CASTEP data base were employed in conjunction with plane waves up to a kinetic energy cutoff of 1020 eV or 630 eV, for norm-conserving and ultrasoft pseudopotentials, respectively. The accuracy of the pseudopotentials is well established.[22] A correction scheme for van der Waals (v.d.W.) interactions was applied in the DFT-calculations. We employed the correction scheme developed by Tkatchenko and Scheffler.[23] A Monkhorst-Pack grid was used for Brillouin zone integrations.[24] We used a distance between grid points of <0.023 Å^{-1}. Convergence criteria for geometry optimization included an energy change of $<5 \times 10^{-6}$ eV atom^{-1} between steps, a maximal force of <0.008 eV Å^{-1} and a maximal component of the stress tensor <0.02 GPa. Phonon frequencies were obtained from density functional perturbation theory (DFPT) calculations.[25,26] Raman intensities were computed using DFPT with the "$2n + 1$" theorem approach.[27] The reliability of calculations of SHG tensors has been established previously.[28]

2. Results

2.1. Single crystal synchrotron X-ray diffraction at 20 GPa

We performed synchrotron single-crystal X-ray diffraction in the area of the gasket hole where we observed mainly Raman modes of the unknown carbonate phase. Fig. S 2 a shows a part of an *unwarped* image of the raw-experimental data after processing of the $(1kl)$ area in CrysAlis, after the location of a suitable spot for the single crystal structure solution. Besides the reflection of the unknown carbonate phase, reflections and powder rings of different CO_2 phases and diamond are present in the diffraction data. Projections of the reciprocal space show the distribution of reflections and the effect of the shading of diffracted beams due to the DAC after data reduction (Fig. S 2 b). The coverage of the reciprocal space is relatively large for a DAC experiment (80% for 0.8 Å^{-1} resolution).

We solved the crystal structure of the unknown carbonate phase in the trigonal space group $P3_121$ (No. 152) with $Z = 3$ and a chemical composition of $Be(CO_3)$. The low R-value of 5.6% is indicative of a reasonable structure refinement. The displacement parameters of the beryllium, the carbon and both oxygen atoms were refined anisotropically. No constraints or restraints were applied for the refinement. The reflection to parameter ratio (8.4:1) is acceptable for a DAC experiment. The crystallographic parameters of $Be(CO_3)$ at 20(2) GPa are listed in Table S 1 and in comparison to data derived from the DFT calculations. Atomic coordinates are listed in Table S 2.

Table S 1: Structural parameters of $Be(CO_3)$ at 20(2) GPa from single crystal structure solution (ambient temperature) in comparison to data derived from DFT calculations (athermal limit).

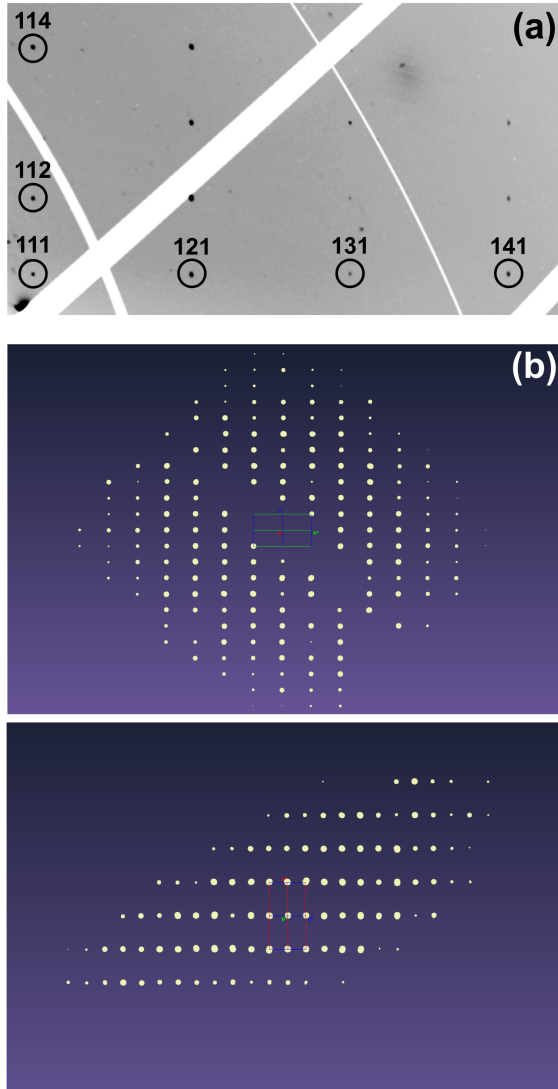|	Single Crystal	DFT
Crystal data		
Crystal system	Trigonal	Trigonal
Space group	$P3_121$	$P3_121$
Chemical formula	$Be(CO_3)$	$Be(CO_3)$
M_r	69.02	69.02
a (Å)	4.0983(7)	4.1553
b (Å)	4.0983(7)	4.1553
c (Å)	7.416(1)	7.5307
α (°)	90.0	90.0
β (°)	90.0	90.0
γ (°)	120.0	120.0
V (Å^3)	107.87(4)	112.61
Z	3	3
Data collection		-
F_{000}	102	-
θ range (°)	3.35–20.26	-
measured reflections	271	-
independent reflections	209	-
reflections $I > 2\sigma(I)$	190	-
R_{int}	0.021	-
		-
Refinement		-
$R[F^2 > 2\sigma(F^2)]$, $wR(F^2)$	0.056, 0.144	-
No. of reflections	209	-
No. of parameters	25	-
No. of restraints	0	-
No. of constraints	0	-
$\Delta\rho_{max}$, $\Delta\rho_{min}$ (e Å^{-3})	0.47, -0.55	-

Figure S 2: (a) *Unwarped* image of the raw-experimental data after data reduction. The $(1kl)$ area is shown. Other reflections are due to other phases present in the sample chamber. (b) Schematic depiction of the reflections in reciprocal space using the Ewald-Explorer in CrysAlis after data reduction which were later used for the refinement. Projections of the reciprocal space are shown along a^* (top) and b^* (bottom).

Table S 2: Atomic coordinates and isotropic displacement parameters of $Be(CO_3)$ at 20(2) GPa obtained by single crystal structure refinement.

Atom	Site	x	y	z	U_{iso} (Å^2)
Be1	3b	0.0	0.8199(12)	1/6	0.0142(8)
C1	3a	0.5800(8)	1.0	1/3	0.0113(7)
O1	3a	0.8945(6)	1.0	1/3	0.0138(6)
O2	6c	0.3172(5)	0.7546(5)	0.2392(3)	0.0138(5)

2.2. Bulk modulus Be(CO₃)

We used the p, V relation obtained from the DFT calculations to calculate the theoretical bulk modulus (K_0) for Be(CO₃). The calculations were carried out between 0 GPa and 50 GPa. We fitted a 3rd-order Birch-Murnaghan equation of states (EoS) to unit cell volume obtained by the calculations (Fig. S 3) using the software package EOSFit7-GUI.[29,30,31]
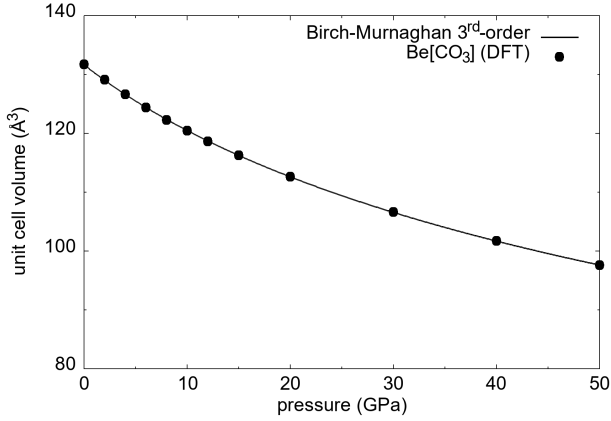

Figure S 3: A Birch-Murnaghan EoS was fitted to the unit cell volumes of Be(CO₃) obtained by DFT-based calculations between 0–50 GPa.

The theoretical bulk modulus of Be(CO₃) derived from the p, V relation is $K_0 = 95.5(8)$ GPa with $K_p = 3.8(1)$. This is in very good agreement with the bulk modulus obtained from our DFT calculations of the elastic stiffness tensor (91(1) GPa).

2.3. Second harmonic generation measurements and DFT calculations

In order to confirm the acentric space group symmetry ($P3_121$) of Be(CO₃) we performed second harmonic generation (SHG) measurements in the DAC at 20(2) GPa . We measured a strong SHG signal (≈ 70 mV) from the sample (Fig. S 4).
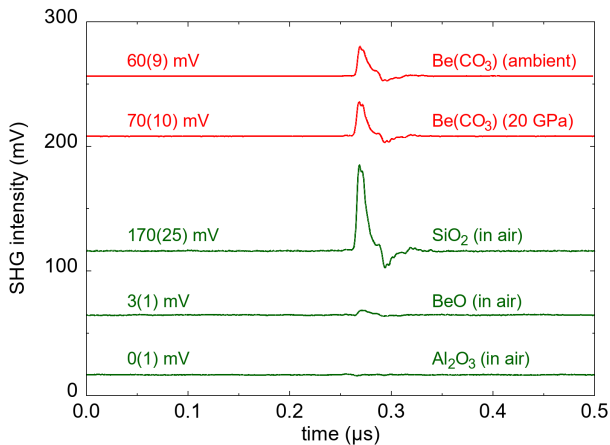

Figure S 4: SHG measurements of Be(CO₃) at 20(2) GPa and ambient conditions in a DAC (red) in comparison to the reference powders quartz (SiO₂), BeO and corundum (Al₂O₃) measured outside a DAC at ambient conditions (green).

The strong SHG signal consistent with our DFT calculations, which reveal a relatively high SHG coefficient of $d_{eff} = 1.34$ pm V^{-1} at 20 GPa. This coefficient is significantly larger than for quartz ($d_{eff} = 0.2$ pm V^{-1}), employed as a reference material outside a DAC here (≈ 170 mV). It is clear to see that no SHG signal can be observed from the centrosymmetric corundum powder. As DFT-GGA-PBE calculations underestimate the band gap, the calculated tensor components will be slightly to large.[28]

$$d_{20\,\mathrm{GPa}} = \begin{pmatrix} 1.936 & -1.936 & 0.000 & 0.000 & 0.000 & 0.000 \\ 0.000 & 0.000 & 0.000 & 0.000 & 0.000 & -1.936 \\ 0.000 & 0.000 & 0.000 & 0.000 & 0.000 & 0.000 \end{pmatrix}$$

$$d_{0\,\mathrm{GPa}} = \begin{pmatrix} 1.342 & -1.342 & 0.000 & 0.000 & 0.000 & 0.000 \\ 0.000 & 0.000 & 0.000 & 0.000 & 0.000 & -1.342 \\ 0.000 & 0.000 & 0.000 & 0.000 & 0.000 & 0.000 \end{pmatrix}$$

As our starting material (BeO) also crystallizes in the acentric space group symmetry $P6_3mc$ some unreacted starting material may still be present in the gasket hole. However the calculated effective SHG coefficient of BeO is four times lower ($d_{eff} = 0.25$ pm V^{-1}) than that of Be(CO₃) at ambient conditions ($d_{eff} = 0.93$ pm V^{-1}). We measured the SHG signal of Be(CO₃) at ambient conditions in a DAC in comparison with pure BeO powder outside a DAC (Fig. S 4). Applying the same laser power we could not detect a significant SHG signal (≈ 3 mV) from BeO, while we receive a strong SHG single from Be(CO₃) (≈ 60 mV) after recovering the sample to ambient conditions. Only at significantly higher laser power a clear SHG signal was detected from BeO. It should be noted, that the grain size of the BeO powder was significantly smaller than the one of the quartz powder, employed as a reference material here.

$$d_{20\,\mathrm{GPa}} = \begin{pmatrix} 0.000 & 0.000 & 0.000 & 0.000 & -0.202 & 0.000 \\ 0.000 & 0.000 & 0.000 & -0.202 & 0.000 & -0.000 \\ -0.202 & 0.202 & -0.210 & 0.000 & 0.000 & 0.000 \end{pmatrix}$$

$$d_{0\,\mathrm{GPa}} = \begin{pmatrix} 0.000 & 0.000 & 0.000 & 0.000 & -0.179 & 0.000 \\ 0.000 & 0.000 & 0.000 & -0.179 & 0.000 & -0.000 \\ -0.179 & 0.179 & -0.281 & 0.000 & 0.000 & 0.000 \end{pmatrix}$$

References

(1) Hazen, R. M.; Finger, L. W. High-pressure and high-temperature crystal chemistry of beryllium oxide. *J. Appl. Phys.* **1986**, *59*, 3728–3733, DOI: 10.1063/1.336756

(2) Boehler, R. New diamond cell for single–crystal X-ray diffraction. *Rev. Sci. Instrum.* **2006**, *77*, 115103–1–115103–3, DOI: 10.1029/JB091iB05p04673

(3) Mao, H. K.; Xu, J.; Bell, P. M. Calibration of the ruby pressure gauge to 800 kbar under quasi-hydrostatic conditions. *J. Geophys. Res.* **1986**, *91*, 4673–4676, DOI: 10.1029/JB091iB05p04673

(4) Spahr, D.; König, J.; Bayarjargal, L.; Luchitskaia, R.; Milman, V.; Perlov, A.; Liermann, H.-P.; Winkler, B.; Synthesis and Structure of Pb[C_2O_5]: An Inorganic Pyrocarbonate Salt. *Inorg. Chem.* **2022**, *61*, 9855–9859, DOI: 10.1021/acs.inorgchem.2c01507

(5) Scelta, D.; Ceppatelli, M.; Ballerini, R.; Hajeb, A.; Peruzzini, M.; Bini, R. Sprayloading: A cryogenic deposition method for diamond anvil cell. *Rev. Sci. Instrum.* **2018**, *89*, 053903, DOI: 10.1063/1.5011286

(6) Bayarjargal, L.; Fruhner, C.-J.; Schrodt, N.; Winkler, B. $CaCO_3$ phase diagram studied with Raman spectroscopy at pressures up to 50 GPa and high temperatures and DFT modeling. *Phys. Earth Planet. Inter.* **2018**, *281*, 31–45, DOI: 10.1016/j.pepi.2018.05.002

(7) Benedetti, L. R.; Loubeyre, P. Temperature gradients, wavelength-dependent emissivity, and accuracy of high and very-high temperatures measured in the laser-heated diamond cell. *High Press. Res.* **2004**, *24*, 423–455, DOI: 10.1080/08957950412331331718

(8) Du, Z.; Amulele, G.; Benedetti, L. R.; Lee, K. K. M. Mapping temperatures and temperature gradients during flash heating in a diamond-anvil cell. *Rev. Sci. Instrum.* **2013**, *84*, 075111, DOI: 10.1063/1.4813704

(9) Wojdyr, M. *Fityk*: a general-purpose peak fitting program. *J. Appl. Cryst.* **2010**, *43*, 1126–1128, DOI: 10.1107/S0021889810030499

(10) Mezouar, M.; Garbarino, G.; Bauchau, S.; Morgenroth, W.; Martel, K.; Petitdemange, S.; Got, P.; Clavel, C.; Moyne, A.; Van Der Kleij, H.-P.; Pakhomova, A.; Wehinger, B.; Gerin, M.; Poreba, T.; Rosa, A.; Forestier, A.; Weck, G.; Datchi, F.; Wilke, M.; Jahn, S.; Andrault, D.; Libon, L.; Pennacchioni, L.; Laniel, D.; Bureau H. The high flux nano-X-ray diffraction, fluorescence and imaging beamline ID27 for science under extreme conditions on the ESRF Extremely Brilliant Source. *High Press. Res.* **2024**, *44*, 171–198, DOI: 10.1080/08957959.2024.2363932

(11) Prescher, C.; Prakapenka, V. B. *DIOPTAS*: a program for reduction of two-dimensional X-ray diffraction data and data exploration. *High. Press. Res.* **2015**, *35*, 223–230, DOI: 10.1080/08957959.2015.1059835

(12) Agilent, CrysAlis PRO, Yarnton, England, **2014**

(13) Aslandukov, A.; Aslandukov, M.; Dubrovinskaia, N.; Dubrovinsky, L. *Domain Auto Finder* (*DAFi*) program: the analysis of single-crystal X-ray diffraction data from polycrystalline sample. *J. Appl. Cryst.* **2022**, *55*, 1383–1391, DOI: 10.1107/S1600576722008081

(14) Dolomanov, O. V.; Bourhis, L. J.; Gildea, R. J.; Howard, J. A. K.; Puschmann, H. *OLEX2*: a complete structure solution, refinement and analysis program. *J. Appl. Cryst.* **2009**, *42*, 339–341, DOI: 10.1107/S0021889808042726

(15) Sheldrick, G. M. *SHELXT* — Integrated space-group and crystal-structure determination. *Acta. Cryst.* **2015**, *A71*, 3–8, DOI: 10.1107/S2053273314026370

(16) Sheldrick, G. M. Crystal structure refinement with *SHELXL. Acta. Cryst.* **2015**, *C71*, 3–8, DOI: 10.1107/S2053229614024218

(17) Bayarjargal, L.; Winkler, B. Second harmonic generation measurements at high pressures on powder samples. *Z. Kristallogr.* **2014**, *229*, 92–100, DOI: 10.1515/zkri-2013-1641

(18) Kurtz, S. K.; Perry, T. T. A Powder Technique for the Evaluation of Nonlinear Optical Materials. *J. Appl. Phys.* **1968**, *39*, 3798–3813, DOI: 10.1063/1.1656857

(19) Hohenberg, P.; Kohn, W. Inhomogeneous Electron Gas. *Phys. Rev.* **1967**, *136*, B864–B871, DOI: 10.1103/PhysRev.136.B864

(20) Perdew, J. P.; Burke, K.; Ernzerhof, M. Generalized Gradient Approximation Made Simple. *Phys. Rev. Lett.* **1996**, *77*, 3865–3868, DOI: 10.1103/PhysRevLett.77.3865

(21) Clark, S. J.; Segall, M. D.; Pickard, C. J.; Hasnip, P. J.; Probert, M. I. J.; Refson, K.; Payne, M. C. First principles methods using CASTEP. *Z. Kristallogr.* **2005**, *220*, 567–570, DOI: 10.1524/zkri.220.5.567.65075

(22) Lejaeghere, K.; Bihlmayer, G.; Björkman, T.; Blaha, P.; Blügel, S.; Blum, V.; Caliste, D.; Castelli, I. E.; Clark, S. J.; Dal Corso, A. et al. Reproducibility in density functional theory calculations of solids. *Science* **2016**, *351*, aad3000, DOI: 10.1126/science.aad3000

(23) Tkatchenko, A.; Scheffler, M. Accurate Molecular Van Der Waals Interactions from Ground-State Electron Density and Free-Atom Reference Data. *Phys. Rev. Lett.* **2009**, *102*, 073005, DOI: 10.1103/PhysRevLett.102.073005

(24) Monkhorst, H. J.; Pack, J. D. Special points for Brillouin-zone integrations. *Phys. Rev. B* **1976**, *13*, 5188–5192, DOI: 10.1103/PhysRevB.13.5188

(25) Baroni, S.; de Gironcoli, S.; Dal Corso, A.; Giannozzi, P. Phonons and related crystal properties from density-functional perturbation theory. *Rev. Mod. Phys.* **2001**, *73*, 515–562, DOI: 10.1103/RevModPhys.73.515

(26) Refson, K.; Tulip, P. R.; Clark, S. J. Variational density-functional perturbation theory for dielectrics and

lattice dynamics. *Phys. Rev. B* **2006**, *73*, 155114, DOI: 10.1103/PhysRevB.73.155114

(27) Miwa, K. Prediction of Raman spectra with ultrasoft pseudopotentials. *Phys. Rev. B* **2011**, *84*, 094304, DOI: 10.1103/PhysRevB.84.094304

(28) Bonnin, M. A.; Bayarjargal, L.; Wolf, S.; Milman, V.; Winkler, B.; Feldmann, C. $GaSeCl_5O$: A Molecular Compound with Very Strong SHG Effect. *Inorg. Chem.* **2021**, *60*, 15653–15658, DOI: 10.1021/acs.inorgchem.1c02315

(29) Murnaghan, F. The Compressibility of Media under Extreme Pressures. *Proc. Natl. Acad. Sci.* **1944**, *30*, 244–247, DOI: 10.1073/pnas.30.9.244

(30) Birch, F. Finite Elastic Strain of Cubic Crystals. *Phys. Rev.* **1947**, *71*, 809–824, DOI: 10.1103/PhysRev.71.809

(31) Gonzalez-Platas, J.; Alvaro, M.; Nestola, F.; Angel, R. *EosFit7-GUI*: a new graphical user interface for equation of state calculations, analyses and teaching. *J. Appl. Cryst.* **2016**, *49*, 1377–1382, DOI: 10.1107/S1600576716008050